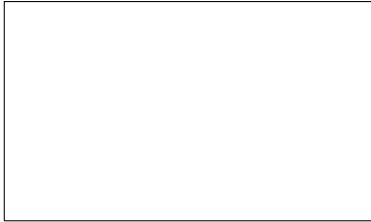


Graphical Abstract

A new Gaussian Process based model for non-linear wave loading on vertical cylinders

Tianning Tang, Gerard Ryan, Haoyu Ding, Xi Chen, Jun Zang, Paul H. Taylor, Thomas A. A. Adcock



Highlights

A new Gaussian Process based model for non-linear wave loading on vertical cylinders

Tianning Tang, Gerard Ryan, Haoyu Ding, Xi Chen, Jun Zang, Paul H. Taylor, Thomas A. A. Adcock

- We establish a new Gaussian Process based model for nonlinear wave loading on a vertical cylinder with a Stokes-type harmonic expansion model based on previous wave group experiments. We further expand the parameter space of the database by designing and performing new experiments in a wave tank.
- Based on this Gaussian Process based model, we establish an engineering prediction model for the nonlinear loading on vertical cylinders using machine learning data assimilation.
- We present a wave-by-wave prediction model of higher harmonics of random wave loads on a surface-piercing column with a wave-group segmentation method, which helps isolate wave groups from the random background.

A new Gaussian Process based model for non-linear wave loading on vertical cylinders

Tianning Tang^a, Gerard Ryan^a, Haoyu Ding^b, Xi Chen^c, Jun Zang^b, Paul H. Taylor^d, Thomas A. A. Adcock^a

^a*Department of Engineering Science, University of Oxford,, Oxford, UK*

^b*Department of Architecture & Civil Engineering, University of Bath, Bath, UK*

^c*Department of Computer Science, University of Bath, Bath, UK*

^d*Oceans Graduate School, The University of Western Australia, Perth, Western Australia*

Abstract

We aim to establish a fast and accurate model for fast prediction of nonlinear loading on vertical cylinders such as are typically used for fixed offshore wind turbines. We follow a ‘Stokes-type’ force model and approximate the amplitude of the higher harmonics of force by relating these to the linear force time series raised to appropriate power through amplitude and phase coefficients. We reanalyse previous experimental data and perform new experiments to expand the parameter space and establish a force coefficients database for engineering applications. A machine learning model is used to interpolate the database and make predictions on the higher order force coefficients. The machine learning model also provides a cross-validated confidence interval to indicate the prediction uncertainty and reflect model reliability. We further extend the prediction capability to unidirectional random waves with a novel force segmentation method, which localised wave groups from the random background. The new Stokes-Gaussian Process (Stokes-GP) model developed can provide engineering predictions of nonlinear wave loading on a cylinder for individual wave groups and random seas, which are straightforward to apply and fast to compute and the important higher-order loading components are considered. This will significantly improve the accuracy of the loading prediction and the ease of application for force predictions.

Keywords: Ocean Engineering, Wave-structure interaction

1. Introduction

Ocean wave loading is one of the dominant environmental forces considered during the design of offshore wind turbines (International Electrotechnical Commission, 2009). At the time of writing monopile structures are still the most common foundation type of wind turbine (Gupta and Basu, 2020; Malekjafarian et al., 2021) and hence the wave loading on a vertical cylinder is of considerable interest. In addition to the linear inertia loading at the same frequencies as the incoming wave field, the nonlinear interaction between the wave and a vertical cylinder leads to higher-order harmonic forces and can contribute a significant amount to the total force magnitude—in steep but realistic sea-states contributing an additional 60% to the peak load (Chen et al., 2018). These higher harmonics may occur at frequencies that are close to the structural natural frequency and are thus of obvious concern given the low damping typical in offshore wind turbines. The third harmonic in particular has been discussed at length in the literature (Faltinsen et al., 1995; Malenica et al., 1995; Rainey, 1995). The loading from higher nonlinear loads will contribute to structural fatigue (Schlører et al., 2016) and the ultimate limit state loads (Wang et al., 2021).

Various theoretical approaches have been developed to understand the non-breaking wave interactions with cylinders and quantify these higher harmonic loads. Theory for wave diffraction based on the classical perturbation expansions up to 2nd order in wave steepness has been developed by numerous authors (e.g. Molin (1979), Eatock Taylor and Hung (1987), and Newman (1996)). Beyond second order diffraction theory, a model generally known as ‘FNV’ after the authors were established to estimate the third-order wave force on a slender cylinder in deep water, assuming that the incident wave amplitude is comparable to the cylinder radius (Faltinsen et al., 1995). This FNV model generally shows good agreement with experimental results within its range of validity (Kristiansen and Faltinsen, 2017; Huseby and Grue, 2000; Chen et al., 2018). Experimental studies of the higher harmonics of wave loading include Stansberg et al. (1995); Chaplin et al. (1997); Huseby and Grue (2000); Grue and Huseby (2002); Riise et al. (2018).

There is thus substantial literature on the fluid mechanics of non-linear wave loads. However, this work is not readily usable in engineering practice. There is a need for a computationally fast and straightforward way of capturing the key non-linear wave dynamics in hydro-aero-elastic models of offshore wind turbines (e.g. OpenFast, Ashes, etc.) (Gupta and Basu, 2020).

The approach we take here is to assume the forces can be modelled with a ‘Stokes-like’ approach where the time history of the total force can be reconstructed as a sum of harmonics approximated based on the underlying linear force time history raised to an appropriate power and with fitted coefficients. This method was first introduced by Chen et al. (2018), extended from force to moments by Feng et al. (2020) and to directionally spread waves by Mj et al. (2023).

In this paper, we aim to establish a Stokes-Gaussian Process model for the higher order force loadings which can then be used for the design of offshore wind turbines. We choose to base this model on experimental data. We revisit previous experimental results which we complement with new experiments to extend and in-fill the parameter space. We first improve the force coefficient extraction procedure following the existing four-phase decomposition method with a data-driven nonlinear fitting and optimisation approach to replace the simple least-squares fitting used previously. With the new force coefficient extraction procedure, we have reanalysed previous results collected from three different experimental campaigns and now establish a higher order force coefficients database dependent on the relative wave properties and cylinder geometry. We compare the second-order coefficients from the database with standard diffraction theory and explore the two reported force non-dimensionalisation approaches used in previous literature (Feng et al., 2020).

We interpolate the existing Stokes-type model data with machine-learning fitted force coefficients to estimate the total nonlinear force based on the linear force as input. We train the machine learning model based on the force coefficients database established previously and test its performance with a new set of experiments performed at the Kelvin Hydrodynamics Laboratory, University of Strathclyde. We further expand the capability of the newly established nonlinear force model to a random wave field through a force segmentation scheme, which isolates individual wave groups from the random background, and avoids the ambiguity of determining the peak wavenumber values. This allows wave-by-wave prediction of the nonlinear forces induced by a unidirectional random wave field. We further establish a cross-validated upper confidence interval to reflect model prediction uncertainty.

This paper is structured as follows. In Section 2, we introduce the experimental setups for the new experimental campaign. We also introduce the Stoke-type force model as well as the data-driven approaches utilised in this study to make predictions on the nonlinear force. In Section 3, we present the

model prediction performance by comparing it to experimental data followed by discussions and conclusions in Section 4.

2. Methods

In principle, we could develop our model on analytical, numerical or experimental results. We choose to base our analysis on the latter. The fluid dynamic interaction of a steep incident wave with a surface piercing column is highly complex, and it is unclear whether all the relevant physics is captured by analytical models—particularly for higher order harmonics. Numerical simulations of the problem are a valuable tool and give rich information on the force distribution on the cylinder, but correctly representing the high-frequency components remains challenging. Thus, we base our analysis on experiments. Of course, these are not without their difficulties, as discussed below, but we believe these give the best representation of wave loading for real-world situations.

2.1. Previous experiments

In this study, we analyse wave group loading from the experimental campaigns of Chen et al. (2018), Mj et al. (2023) and Feng et al. (2020). We describe these as the ‘LC18’, ‘DM22’ and ‘XF20’ respectively. We describe the detailed experimental setup of each previous experimental campaign in Appendix A and we summarise the main features of each past experiment in Table 1.

We have selected these experiments from the large literature on the topic for a variety of reasons. Firstly, the data was available and well documented as members of the present project had worked on these studies. This also meant that we had a good idea of the short-comings and issues with these experiments which we could then attempt to account for in our new analysis. In particular, we are keen that different harmonics should be cleanly

Table 1: Comparison of previous experiments and new experiments.

Name	Data type	Bottom Profile	No. of sea-states	Directionality
MJ23	Random waves	Flat bed	11+6	Unidirectional and Directional spread
XF20 Group	Wave groups	Flat bed	6	Unidirectional
XF20 Random	Random waves	Flat bed	1	Unidirectional
LC18 (Group flat)	Wave groups	Flat bed	12	Unidirectional
LC18 (Group slope)	Wave groups	1-in-20 slope	16	Unidirectional
New Exp Group	Wave groups	Flat bed	22	Unidirectional
New Exp Random	Random waves	Flat bed	3	Unidirectional

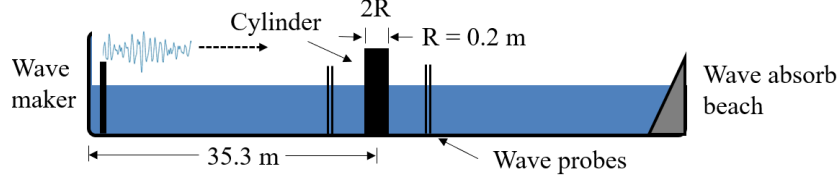


Figure 1: Experimental setup for experiments at Kelvin Hydrodynamics Laboratory, the University of Strathclyde.

extracted and that the inevitable structural dynamics of the cylinder in the experimental campaigns are accounted for.

2.2. New experiments

We perform a new set of experiments in the large flume (76 m long, 4.6 m wide with a constant water depth of 1.8 m) at the Kelvin Hydrodynamics Laboratory, the University of Strathclyde. A single bottom-mounted surface-piercing vertical cylinder with a radius (R) of 0.2 m was placed 35.3 m away from the wavemaker (see Figure 1 for layout details). In all the experimental cases, the diameter of the monopile is sufficiently large so that the wave-induced forces are dominated by inertial loading. The in-line component of the wave force was measured by load cells installed at the junction connecting the cylinder and the support frame. Three wave probes are installed in the front, out to the side in-line with the centre, and at the back of the cylinder. However, we define the wave field in terms of the undisturbed record measured at the position of the centre of the cylinder but with the cylinder removed (i.e. empty tank test). This avoids having any scattered wave components in the incoming wave description.

Focused wave groups and random waves are generated by ‘flap-type’ wave-makers and follow the JONSWAP spectrum ($\gamma = 3.3$). The detailed parameters of generated wave groups and random sea states are shown in Table 2 and Table 3 respectively. Extra cases are also performed during this experimental campaign. The parameters for these experiments were determined using a machine learning algorithm so as to fill out the parameter space as efficiently as possible. This algorithm is presented in Tang et al. (2023b).

For all of the focused wave groups, an iterative focused wave group generation method is applied following Chaplin (1996) to ensure the phases of all the frequency components are aligned at the cylinder centre. A hammer test

Table 2: Incoming wave fields as input signal for new wave group experiments, where d is water depth, and R is cylinder radius. f_p is peak frequency, k_p is the peak wave number associated with the peak period and A is wave group amplitude.

WaveRunID	f_p (Hz)	A (m)	T_p (s)	$k_p A$	$k_p R$	$k_p d$
1	0.40	0.20	2.50	0.13	0.13	1.16
2	0.40	0.15	2.50	0.10	0.13	1.16
3	0.40	0.16	2.50	0.10	0.13	1.16
4	0.40	0.18	2.50	0.12	0.13	1.16
5	0.40	0.19	2.50	0.12	0.13	1.16
6	0.40	0.23	2.50	0.15	0.13	1.16
7	0.40	0.27	2.50	0.17	0.13	1.16
8	0.40	0.29	2.50	0.19	0.13	1.16
9	0.34	0.18	2.94	0.08	0.09	0.84
10	0.34	0.23	2.94	0.11	0.09	0.84
11	0.34	0.27	2.94	0.13	0.09	0.84
12	0.34	0.32	2.94	0.15	0.09	0.84
13	0.39	0.12	2.56	0.07	0.12	1.10
14	0.39	0.17	2.56	0.10	0.12	1.10
15	0.39	0.23	2.56	0.14	0.12	1.10
16	0.39	0.28	2.56	0.17	0.12	1.10
17	0.54	0.12	1.85	0.14	0.23	2.11
18	0.54	0.17	1.85	0.20	0.23	2.11
19	0.54	0.23	1.85	0.27	0.23	2.11
20	0.61	0.09	1.64	0.13	0.30	2.69
21	0.61	0.11	1.64	0.16	0.30	2.69
22	0.61	0.12	1.64	0.18	0.30	2.69
23	0.71	0.08	1.40	0.19	0.41	3.64

Table 3: Incoming wave fields as input signal for random waves during the new experiments. H_s is significant wave height, T_p is peak wave period, d is water depth, k is peak wave number associated with peak wave period and R is cylinder radius

Wave field ID	H_s (m)	T_p (s)	k_p [m^{-1}]	$1/2 H_s k_p$	$k_p R$	$k_p d$
Run01	0.22	2.78	0.64	0.07	0.13	1.15
Run02	0.20	1.70	1.41	0.14	0.28	2.54
Run03	0.10	1.27	2.50	0.13	0.50	4.49

was performed to obtain the natural frequency of the cylinder and supporting frame system. The natural frequency of the system is around 8 Hz, which is between 13 and 21 times the frequency of peak wave spectral energy. A simple transfer function is applied to remove the structural responses following Chen et al. (2018), although the resonance is clearly significantly higher than the frequencies we are primarily interested in.

2.3. Stokes-GP: a higher order force model with machine learning fitted coefficients

We propose a Stokes-Gaussian Processes model (Stokes-GP hereafter) for predicting the higher frequency components of wave loading on the cylinder. We first follow the four-phase harmonic extraction method detailed in Section 2.3.1. This method allows the separation of nonlinear forces into different harmonics in frequency by repeating the experiments with four different phases. These harmonics are then fitted with Stokes type expansion form with the nonlinear data fitting and optimisation approach in Section 2.3.2. We finally introduce the Gaussian Process, which interpolates the extracted force coefficients in Section 2.3.3 for prediction purposes.

2.3.1. Harmonic components extraction and Stokes type force model

In this paper, we utilise the Stokes-type force model to make predictions on higher force harmonics based on the linear wave force time-history only (Chen et al., 2018). With the assumption of a narrow-banded spectrum, the waves can be assumed to have a slowly varying envelope $\hat{\mathcal{F}}_1$, and we assume the total wave force up to the 4th harmonic can be written as:

$$F = \hat{\mathcal{F}}_1 \cos(\varphi) + \hat{\mathcal{F}}_1^2 F_2 \cos(2\varphi + \Phi_2) + \hat{\mathcal{F}}_1^3 F_3 \cos(3\varphi + \Phi_3) + \hat{\mathcal{F}}_1^4 F_4 \cos(4\varphi + \Phi_4) + O(\hat{\mathcal{F}}_1^5) \quad (1)$$

where $\hat{\mathcal{F}}_1$ is the envelope of the linear force, φ is the phase of the higher order harmonics, which can be obtained from the signal and its Hilbert transform. F_n represents the amplitude coefficients for the n^{th} order of force harmonics and Φ_n is the phase coefficients for the n^{th} order of force.

We follow the ‘phase separation’ first described in Fitzgerald et al. (2014) (building on the two phase approach of Baldock et al. (1996)) to obtain the higher frequency force components of wave loading. The four-phase decomposition method is based on the form of a generalised Stokes expansion,

where the force is expressed originally for regular wave trains. With this four-phase decomposition approach, we primarily aimed at isolating the super harmonic contributions from each other as they are of most interest and have a significant contribution to the total force.

The phase decomposition method requires repeating the experiment with carefully controlled phase shifts at 0, 90, 180, and 270 degrees. One key component of using this approach in experiments is to keep phase alignment for repeated cases with different relative phase shifts. This is relatively straightforward for wave groups as wave breaking can be closely monitored and reflected waves can be excluded from the analysis. For random waves, previous studies have shown wave breaking and reflections may affect the phase alignment, especially for long runs (Adcock et al., 2019), as the loss of coherence between the phases could accumulate over time and affect the force decomposition. As such, we have chosen a relatively short experimental duration (15 minutes) with four separate runs with different sets of random phases and amplitudes to ensure high-quality separation of the higher-order harmonics is achieved during the experiments.

Following the phase decomposition method described in Feng et al. (2020), we can linearly combine the four corresponding responses ($\mathcal{F}_0, \mathcal{F}_{90}, \mathcal{F}_{180}, \mathcal{F}_{270}$) with successive phase angles lagged by 90 degrees to obtain the higher-order harmonics as:

$$\begin{aligned}
\left(\hat{\mathcal{F}}_1 F_{11} + \hat{\mathcal{F}}_1^3 F_{31}\right) \cos \varphi + O\left(\hat{\mathcal{F}}_1^5\right) &= \left(\mathcal{F}_0 - \mathcal{F}_{90}^H - \mathcal{F}_{180} + \mathcal{F}_{270}^H\right) / 4, \\
\left(\hat{\mathcal{F}}_1^2 F_{22} + \hat{\mathcal{F}}_1^4 F_{42}\right) \cos 2\varphi + O\left(\hat{\mathcal{F}}_1^6\right) &= \left(\mathcal{F}_0 - \mathcal{F}_{90} + \mathcal{F}_{180} - \mathcal{F}_{270}\right) / 4, \\
\hat{\mathcal{F}}_1^3 F_{33} \cos 3\varphi + O\left(\hat{\mathcal{F}}_1^5\right) &= \left(\mathcal{F}_0 + \mathcal{F}_{90}^H - \mathcal{F}_{180} - \mathcal{F}_{270}^H\right) / 4, \\
\hat{\mathcal{F}}_1^2 F_{20} + \hat{\mathcal{F}}_1^4 F_{40} + \hat{\mathcal{F}}_1^4 F_{44} \cos 4\varphi + O\left(\hat{\mathcal{F}}_1^6\right) &= \left(\mathcal{F}_0 + \mathcal{F}_{90} + \mathcal{F}_{180} + \mathcal{F}_{270}\right) / 4,
\end{aligned} \tag{2}$$

where the expansion is truncated at the fourth order and the superscript H denotes the Hilbert transform of the relevant time signal.

We demonstrate this phase manipulation method following Equation (2) and present an example of separated higher order harmonic forces in Figure 2 (a), where we find the four-phase decomposition method is capable of isolating the higher order harmonics for the experimental data. After obtaining these composite time series, we can extract the harmonics through straightforward frequency filtering, as there is minimal overlap between adjacent harmonics in the frequency content. We follow the filtering method

explained in Mj et al. (2023) and present the energy content in Figure 2 (*b*), where we show a clean separation of the force energy content up to fifth-order harmonics.

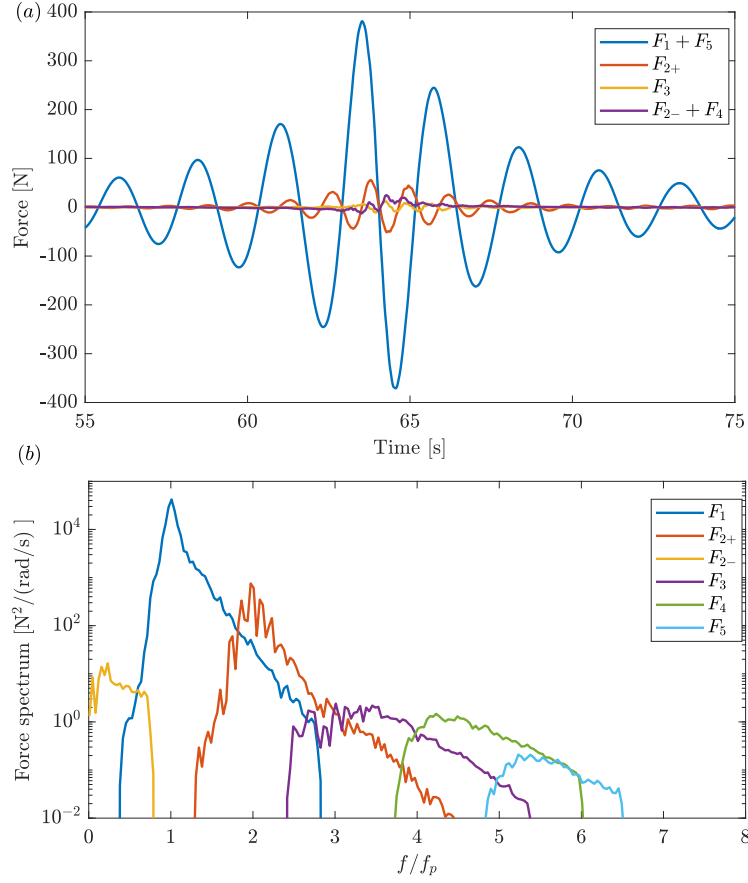


Figure 2: Demonstration of four phase decomposition method: (a) The harmonic structures of horizontal wave loading on the cylinder and the envelopes of case 4 (b) The filtered force spectra for the corresponding focused wave group and forces.

2.3.2. Force coefficients extraction and optimisation

Instead of following the linear least square fitting method to obtain the force amplitude and phase coefficients used in Chen et al. (2018) and by Feng et al. (2020), we adopted a Nelder-Mead simplex algorithm to obtain a better estimate of force amplitude coefficients according to the form of Stokes-type expansion. The general approach is illustrated in Figure 3.

We placed an extra step (i.e. phase 2 in the graph) at the end of the non-linear force extraction process, which aims at optimising the overall model performance on the total wave force. This optimisation scheme utilises the gradient descent algorithm (Ruder, 2016) to tune the force amplitude coefficients aiming at an improved representation of the total nonlinear force. We also adopted the estimated nonlinear fitted coefficients as the initial conditions of our iterative optimisation scheme, which allows a better convergence towards the optimal combination of the coefficients. We report the improvement with this optimisation method on the total nonlinear force predictions in Section 3.1.3.

2.3.3. Force coefficients predictions with Gaussian process

We propose to use the Gaussian Process (GP) method to replace the polynomial fitting algorithm and obtain a better estimation of force amplitude coefficients. The essentials of what we are trying to achieve are given by

$$F_n \sim \mathcal{GP}(k_p A, k_p d, k_p R), \quad (3)$$

where $k_p A$ is the nondimensional wave amplitude, $k d$ is the nondimensional water depth and $k_p R$ is the nondimensional cylinder slenderness. We train

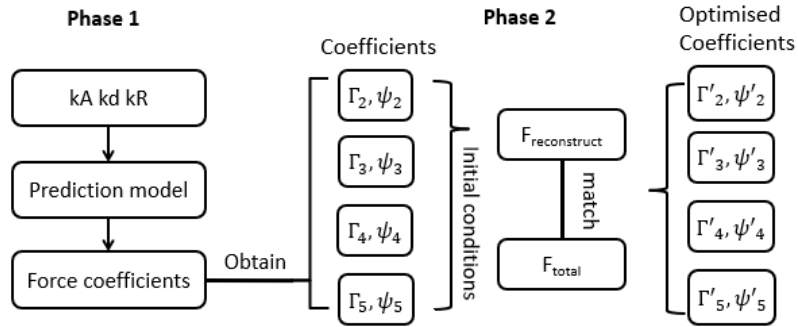


Figure 3: General architecture of coefficient extraction and optimisation

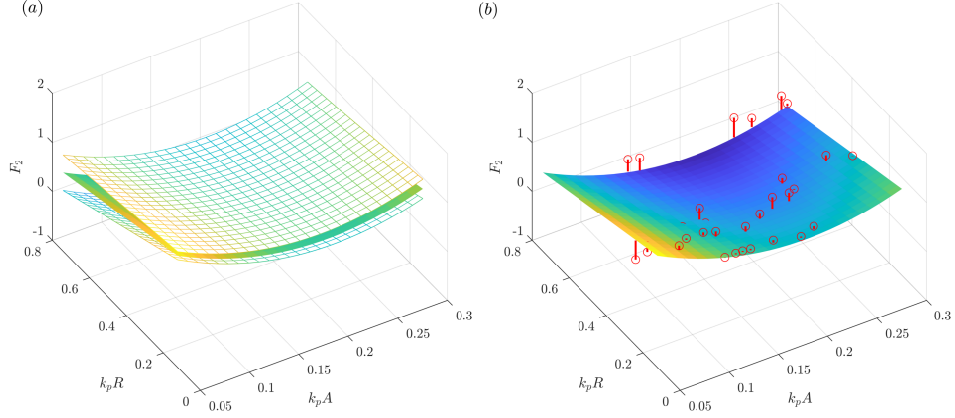


Figure 4: GP based force coefficients prediction in $k_p A$ and $k_p R$ domain: (a): the confidence interval, and (b): comparison to experimental data (red circles), the vertical red lines indicate the difference between the experimental data and GP based force coefficients prediction results.

the GP model with the reanalysed higher-order force coefficients obtained from past experimental results using the extraction method detailed in 2.3.1.

The detailed setup and training of GP model are listed in Appendix B. An example of GP-fitted second-order force coefficients is presented in Figure 4 (b). From the model prediction residual indicated by the red vertical lines, the interpolation model can predict the force amplitude coefficients for higher-order harmonics relatively well for the majority of the experimental cases. Some significant prediction residuals can be observed for large $k_p R$ values, which is likely due to the lack of data samples for relatively large cylinder cases and the more complicated behaviour of wave diffraction for larger cylinders. This is further supported by the large confidence interval produced by the GP model based on the covariance matrix for large $k_p R$ predictions. This approach outperforms standard interpolation techniques such as polynomial fitting as demonstrated in section 3.1.3.

3. Results

We first explore the nonlinear inline force measured in our new experiments and the associated higher frequency forces. We compare our new experimental results against previous experiments as well as standard diffraction theory in Section 3.1.1 and Section 3.1.2. We further demonstrate the

accuracy of the Stokes type expansion model with machine learning fitted coefficients in Section 3.1.3, and then extend the model capability to include the analysis of random fields in 3.2.

3.1. Wave groups

3.1.1. Force nondimensionalisation and comparison to diffraction theory

We first investigate the effect of different force normalisation methods on the accuracy of the final extracted coefficients. We start with a set of higher order force harmonics that are nondimensionalised following Huseby and Grue (2000):

$$\hat{F}_n \approx \frac{\mathcal{F}_n}{(2\pi)^{(2-n)}\rho g A^n R^{(3-n)}} \quad (4)$$

where A is the wave amplitude. Following Mj et al. (2023), A can be estimated based on the first order inertial wave loading equations:

$$F_1 = C_M \pi \rho g A R^2 \tanh(kd), \quad (5)$$

where C_M is the inertial loading coefficient, g is gravitational acceleration and ρ is the density of water. We follow Mj et al. (2023) and take the C_M for cylinders as 2, the linear potential flow value. This gives the wave amplitude A associated with the linear inline force as:

$$A \sim \frac{\max(F_1)}{2\pi\rho g R^2}. \quad (6)$$

Note that there is a phasing difference between surface elevation and the inline forces meaning the maximum of these will occur at different times. To mitigate this effect, we work on the maximum value of the envelope of the time-history signals instead of the phase-resolved one.

Alternatively, following the original definition of the A , we can estimate the wave amplitude by taking the maximum of linearised surface elevation η_L measured at the centre position of the cylinder with the absence of the cylinder (empty tank or no cylinder test):

$$A \sim \max(\eta_L). \quad (7)$$

We note that it is also possible to estimate wave group amplitude A from Fourier coefficients under linear evolution assumptions. In this study, however, the nonlinear evolution of the wave group can lead to an increase in

wave group amplitude at the cylinder (Adcock and Yan, 2010; Esandi et al., 2020). The nonlinear evolution depends on the travelling distance and is site-specific, which makes direct estimation of wave group amplitude A from Fourier amplitude coefficients challenging.

In Figure 5, We present our results with two different normalisation methods described above. The diffraction calculation results are adapted from the work Chen et al. (2018), which is based on the second order diffraction theory following Eatock Taylor and Chau (1991); Zang et al. (2006). For the first-order harmonics, only the second normalisation method (i.e. following Equation (7) is applicable and hence examined herein. Several experiments with the same wavenumbers (also periods) are grouped in the plot, and the variation is estimated from the standard deviation within each group. We report overall good agreement from all experiments with the diffraction theory over a wide range of $k_p R$ values for the linear loading, indicating standard diffraction calculations are suitable for the wave and loading conditions considered in this work. Additionally, the standard diffraction calculation is performed based on regular waves at peak frequency, which is challenging to estimate for waves associated with a range of frequencies, so some deviation from the calculation is expected.

The overall trend in the normalised second-order force coefficients also shows a similar behaviour as the second-order diffraction calculations for different sets of experiments. We report the force being normalised by the maximum linear force amplitude F_1 seems to produce higher force amplitude coefficients when compared to those normalised by empty tank wave amplitude A . This discrepancy seems to be more pronounced for relatively smaller $k_p R$ values, which suggests these long wave or small cylinder loadings are more sensitive to the choice of force nondimensionalisation method. In this long wave region, the normalisation method with the maximum linear force amplitude F_1 seems to agree better with the second order diffraction theory calculations and we adopted this nominalisation approach in this study. The other point towards the choice between A and F_1 is the value taken for inertial loading coefficient C_M , where the linear Morison Equation and many other engineering models (e.g. Rainey (1995)) used as 2, which could be different in practice.

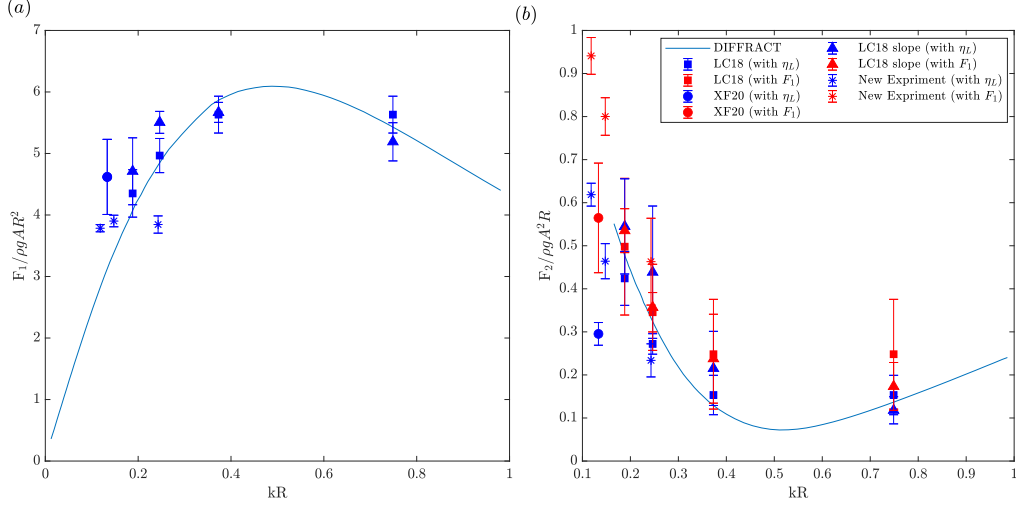


Figure 5: Variation of non-dimensional first- and second-order force harmonics with the cylinder size $k_p R$, for (a) first order coefficients and (b) second order coefficients. The DIFFRACT calculations is adopted from Chen et al. (2018).

3.1.2. Overall performance of Stokes-GP model

We first provide an overview of the Stokes-GP model performance across various wave input conditions. In Figure 6 (a), we present the scatter plot of the wave group parameters based on both previous and new experimental data in the $k_p d$ vs. $k_p R$ plane. We have also adapted the hourly distribution of sea-state parameters for all 36 locations of UK offshore wind farms from Tang et al. (2023a) to provide a direct comparison of the parameter space coverage between our coefficient database and real-world engineering applications.

A striped pattern was observed from the field data, as the water depth (d) to monopile radius (R) ratio is typically fixed per wind farm. Apart from a few wind farms that have large depth-to-radius ratios (d/R) at the top left corner, depth-to-radius ratios (d/R) are clustered in the right bottom corner for most of the wind farms. This pattern suggests an important range in the parameter space that matches the realistic sea-state conditions around UK wind farms.

Although our database provides reasonable coverage of this critical region, there is a clear limitation in the number of depth-to-radius ratios (d/R) that can be explored experimentally. This limitation is primarily due to the depth-

Table 4: Parameter space for four test cases shown in Figure 6.

Test Case	Case Name	$f_p[Hz]$	$A[m]$	$k_p A$	$k_p d$	$k_p R$
1	New11	0.34	0.27	0.13	0.84	0.09
2	New04	0.40	0.18	0.12	1.16	0.13
3	New23	0.71	0.08	0.16	3.64	0.41
4	LC10	1.22	0.02	0.14	3.04	0.75

to-radius ratio being solely dependent on the experimental conditions and typically being fixed for each experimental campaign. Our database tends to focus on relatively 'long' waves with small k_p values, as these cases are prioritised for limited tank time considering both scientific interests and the extreme loading conditions during severe winter storms.

To provide an overview of the Stokes-GP model performance, we selected four cases at the edge of the parameter space and compared the predictions from the Stokes-GP model with the measured force for each, as shown in Figure 6 ($b - e$). Overall, the Stokes-GP model provides accurate predictions across the parameter space and can accurately predict both the phase and amplitude of the total inline force, even though poorer performance is expected at the edge of the parameter space due to insufficient training data and model extrapolation. For cases with larger $k_p R$ values, a slightly larger discrepancy between the Stokes-GP model prediction and the measured force is observed. This discrepancy could be due to the fact that there might be additional nonlinear physics not fitting the Stokes-type model (see also discussions in Kristiansen and Faltinsen (2017)).

The four cases presented in Figure 6 ($b - e$) are adapted from different experimental campaigns with different test facilities and scaling factors. This demonstrates that the force nondimensionalisation for the Stokes-GP model, as discussed in Section 3.1.1, is capable of accommodating different scales of the wave-cylinder interaction. Furthermore, it shows that the generalized Stokes-GP model is robust to input data from different sources.

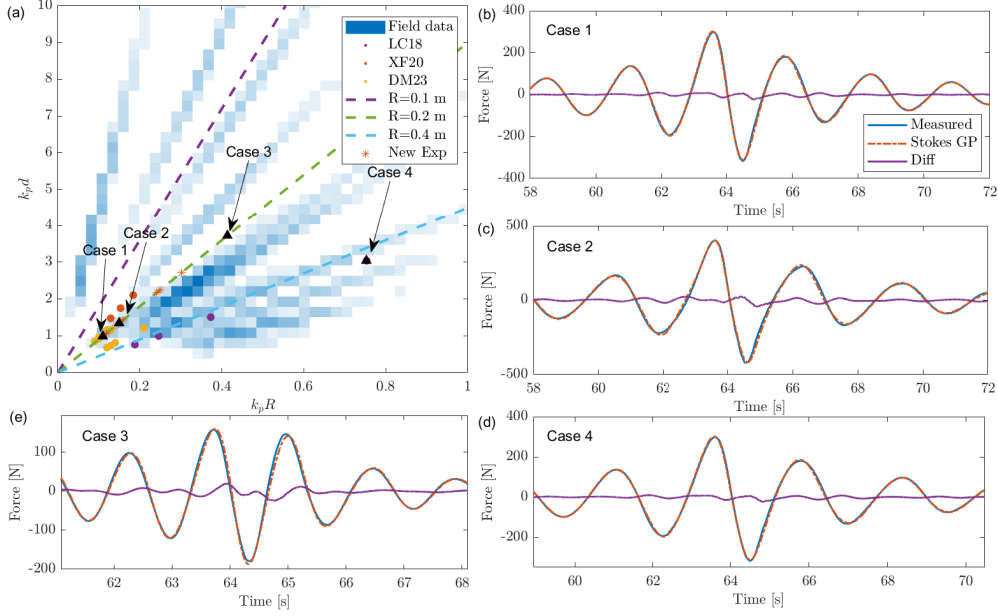


Figure 6: Overview of force prediction capability of Stokes-GP method at various positions in the parameter space. The field data distribution in (a) is adapted from Tang et al. (2023a) for 36 locations of UK offshore wind farms between 2004 and 2024. Panel (b – e) compares the Stokes-GP model with experimentally measured total inline force at various locations. The detailed values of $k_p A$, $k_p d$ and $k_p R$ is shown in Table 4

3.1.3. Stokes-GP model predictions for higher harmonics

This section presents the performance of the Stokes-GP approach for higher harmonic forces, comparing our model with experimental measurements which we take as ground truth. Figure 7 (a) shows the coefficient extraction results using both least square fitting and an improved Nelder-Mead simplex algorithm. Both methods accurately extract the higher frequency forces except for the third order harmonics, where the Stokes-type force model appears to deviate from the measured force. This deviation is also likely to be the reason for the slightly large coefficient scattering, which is also consistent with observations in previous studies (Fitzgerald et al., 2014). A recent study connects a similar deviation from the FNV theory at third order with the flow separation and the local runup on the rear side of the cylinder based on regular wave experiments (Kristiansen and Faltinsen, 2017), although we note the deviation was also found in Fitzgerald et al.

(2014) whose boundary-element potential flow model would not have captured viscous separation.

Figure 7 (b) presents a detailed analysis of the model performance, comparing the GP-based coefficient fitting method with empirical fitting models such as standard polynomial fitting. Our findings indicate that both methods predict the second-order force harmonics relatively accurately. However, the polynomial surface fitting fails to predict higher-order harmonics. This is primarily because the high dimensional parameter space (i.e., three parameters with $k_p R$, $k_p d$ and $k_p A$), imposes challenges in the traditional fitting method with an ill-conditioned weight matrix. This ill-conditioned weight matrix significantly impacts the model accuracy when limited observations are available, or the collected data is associated with higher levels of noise (e.g., the noise is more pronounced for fifth-order harmonics). In contrast, data-driven methods such as GP-based coefficient fitting utilize this information in a more efficient manner and can achieve better results even up to fifth-order force harmonics.

In addition to the comparison between the GP-based coefficient fitting method and empirical fitting models, we also investigated the improvements achieved by introducing the optimisation of the total force. Figure 8 shows the improvements of the prediction on the maximum force peak values in the mean wave direction quantified by the relative prediction error. The optimisation sequence focused on improving the prediction of the total nonlinear force and achieved slightly better prediction results, which is important for extreme loading calculations.

In Figure 9 (a), we present the final prediction results obtained by combining nonlinear fitting, optimisation, and GP interpolated coefficients. The predictions from the Stokes-GP prediction model agree well with the measured force. In Figure 9 (b), we separate the total force into different higher-frequency components up to the 5th order and compare the extracted higher-order harmonics with the measured forces. The fitted force based on the Stoke-type force model is also presented in red. We observe good agreement between the extracted higher-order harmonics and the measured forces, except for the 3rd harmonic, where the Stokes-type force model seems to deviate from the measured force. This deviation during the fitting stage may be attributed to additional nonlinear physics (Kristiansen and Faltinsen, 2017).

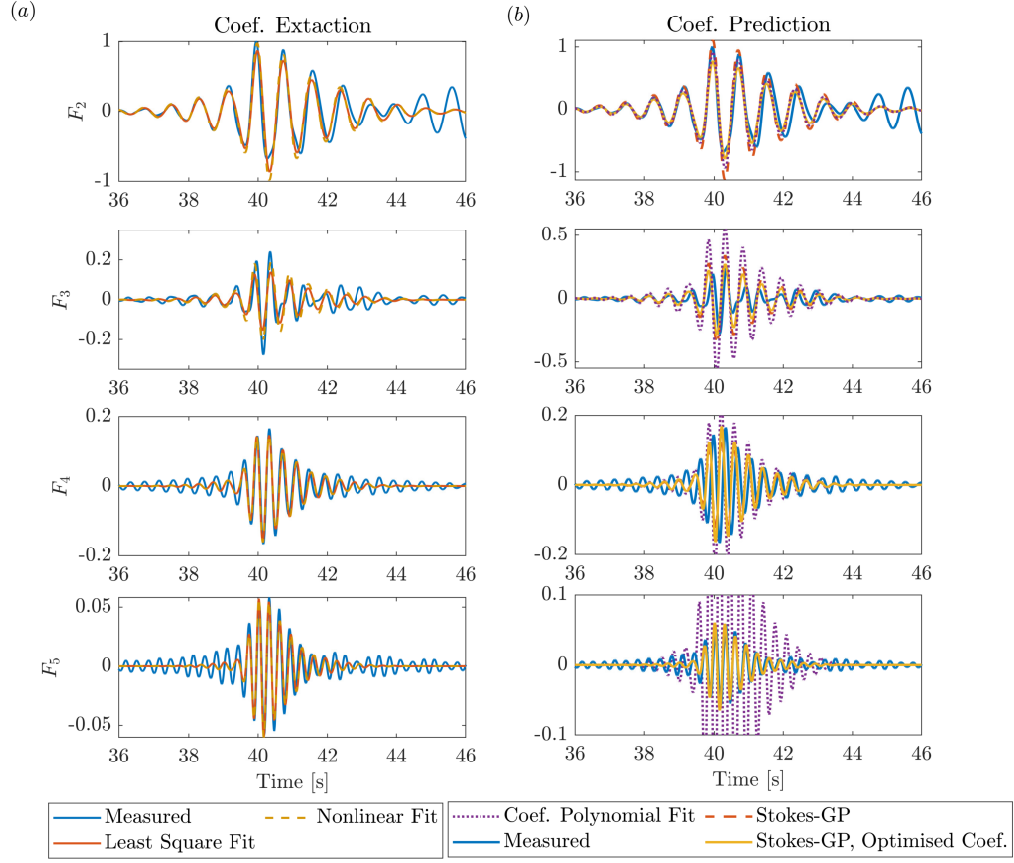


Figure 7: Higher order force harmonics of a wave group LC08 ($k_p A = 0.22$, $k_p R = 0.37$ and $k_p d = 1.51$) (a): force coefficient extraction methods lease square method and Nelder-Mead simplex algorithm, (b): force amplitude coefficients prediction with polynomial fitting and Stokes-GP methods.

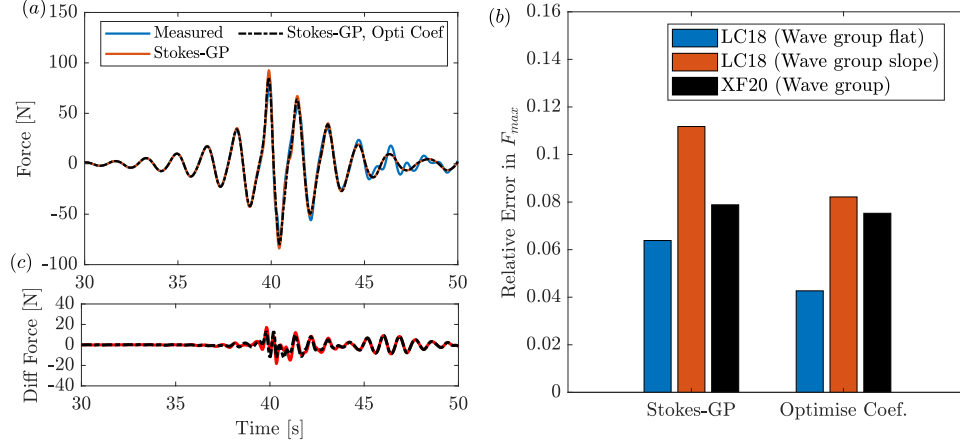


Figure 8: Stokes-GP model predictions for (a): LC08 case ($k_p A = 0.22$, $k_p R = 0.37$ and $k_p d = 1.51$) with and without force coefficient optimisation, (b) overall accuracy comparison of the relative error in maximum nonlinear force predictions for LC18 and XF20 datasets, (c) the difference between the predictions and measured force of LC18 case with and without force coefficient optimisation,

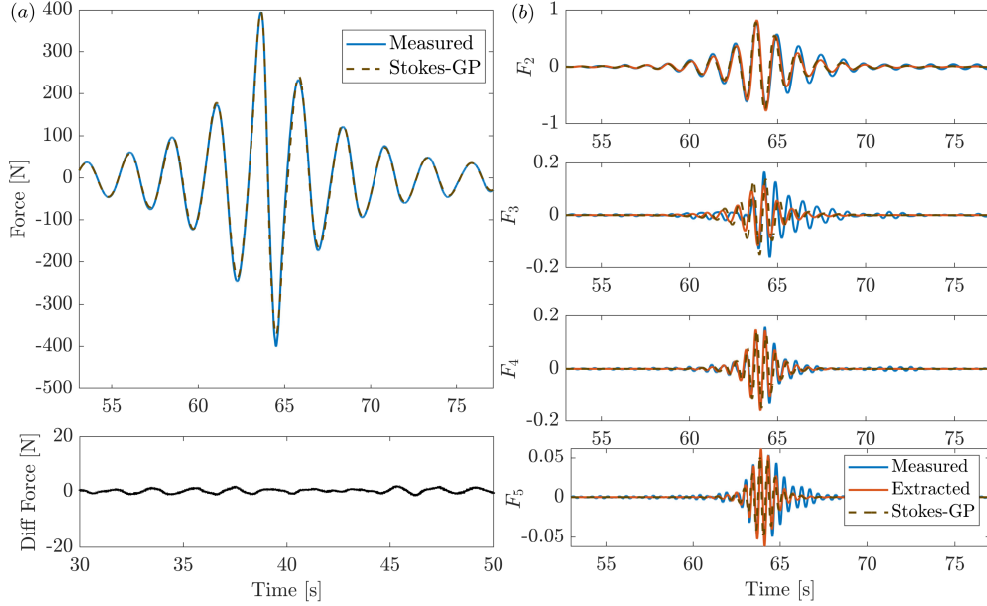


Figure 9: Stokes type model predictions of nonlinear forces for (a): total inline forces, (b): higher order harmonics of a wave group with $k_p A = 0.12$, $k_p R = 0.13$ and $k_p d = 1.16$, (c): the difference between the model predicted force and the measured total inline force. The higher order forces presented in *b* are nondimensionalised according to Eqn. 4.

3.1.4. Comparison with other nonlinear force models

We compare our Stokes-GP model with other existing alternative force models in Figure 10 in an industrial application context. This case study will provide an example deployment of the proposed model in engineering design workflow with the predictions from alternative force models will also be provided. We hope this case study provides a general introduction to Stokes-GP model behaviour in real engineering design situations.

In this case study, we consider a deterministic wave group loading case with a cylinder radius of 4.5m, water depth of 45 m, and a peak period of 13.5 seconds following a JONSWAP spectrum ($\gamma = 3.3$). The largest crest in the numerical simulation is 6.5 m, which gives a local nondimensionalised wave linear focus amplitude of $k_p A = 0.174$. This example is chosen to be representative.

We use the Rainey force model (Rainey, 1995) as one of the nonlinear force models for comparison. The total inline force F_x can be obtained through a depth integration from the bottom $-d$ to free surface η as:

$$F_{\text{Rainey}} = \int_{-h}^{\eta} \left(\rho \pi R^2 \left(2 \frac{\partial u}{\partial t} + u \frac{\partial u}{\partial x} + 2w \frac{\partial u}{\partial z} \right) \right) dz + F^\eta. \quad (8)$$

where u is the horizontal velocity, w is the vertical velocity and ρ is water density, R is cylinder radius, we take the value of $C_m = 2$ in this calculation and the point load F^η includes the surface intersection force which can be calculated as:

$$F^\eta = -\frac{1}{2} \rho \pi R^2 u^2 \frac{\partial \eta}{\partial x} \Big|_{z=\eta}. \quad (9)$$

Similar approaches to estimating the nonlinear force from wave kinematics have been used in past studies (Suja-Thauvin et al., 2020; Jiang and el Moctar, 2022). These results show that the Rainey force model, coupled with fully nonlinear wave kinematics, can provide reasonably accurate force prediction results, although the ‘strong’ nonlinear effects, such as wave slamming and secondary load cycles, are not modelled. However, the Rainey model does not necessarily capture all the relevant physics and the purpose of using it here is as a comparison not because it is a ground truth (Tromans et al., 2006). We also consider the ‘FNV’ model presented in Kristiansen and Faltinsen (2017):

$$F_{\text{FNV}} = \int_{-h}^{\eta} \left(\rho \pi R^2 \left(2 \frac{\partial u}{\partial t} + u \frac{\partial u}{\partial x} + 2w \frac{\partial u}{\partial z} \right) \right) dz + F^\psi, \quad (10)$$

where we take the value of $C_m = 2$ in this calculation. F^ψ is a point load due to the scattered potential and is applied at $z = 0$:

$$F^\psi = \rho\pi R^2 \frac{4}{g} u^2 \frac{\partial u}{\partial t} \Big|_{z=0}. \quad (11)$$

We use first-order Taylor expansions to obtain the kinematics at the $z = 0$ following Suja-Thauvin et al. (2020).

In addition, we consider the simpler cases of using the inertia coefficient from the Morison equation using kinematics from a linear calculation as well as a linear calculation but with Wheeler stretching (Wheeler, 1970). In this approach, linear kinematics are calculated up to mean water level, and the entire profile is stretched from the sea bed vertically up the position of the linear estimated free-surface, which is the standard industry model at present (Nestegård et al., 2006).

For the Rainey and FNV calculations, the nonlinear force is calculated based on highly accurate undisturbed wave kinematics obtained by solving the standard potential-flow water-wave equations using OceanWave3D (details provided in Engsig-Karup et al. (2009)). We simulate the evolution of the wave group at a spatial resolution of 3.6 m (approximately 63 nodes per peak wavelength of 236 m, and also f_p around 0.074 Hz, water depth 45 m), using 60 clustered nodes vertically in the water column. The total simulation time is 540 s, with a time step of 0.2 s (65.5 per peak period). We use a large spatial domain to ensure the wave group does not reach the boundary during the simulation, and we extract the wave kinematics when the wave group amplitude is at its maximum. Four-phase decomposition is used to estimate the linear surface elevation which is then used to derive the kinematics for the more engineering based models.

We first compare the force time-histories of the models in Figure 10 (a). For the largest positive force in the mean-wave direction, there is close agreement between all models, except that the FNV formulation tends to give large predictions of the peak when compared to the Stokes-GP predictions. For force peaks in opposing-wave direction, the models agree except that the FNV formulation tend to over-predict the local value. We present the frequency domain comparison in Figure 10 (b). The Wheeler stretching method tends to overestimate the force amplitude in the linear frequency range but underestimates significantly for the high-frequency components. Particularly around $2f_p$, the Wheeler stretching method predicts 50% less energy than the Stokes-GP model, whereas both the Rainey and FNV force models show less

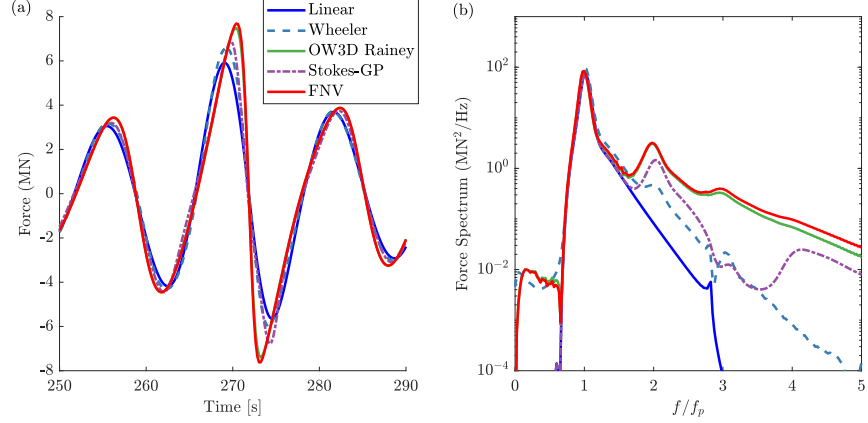


Figure 10: Comparison between Stokes-GP model (purple) and other commonly adopted nonlinear force models: Wheeler stretching method (blue-dash), Rainey (green), and FNV (red) calculated based on kinematics obtained from fully nonlinear potential flow simulations for (a): total inline forces, (b): force spectrum for a wave group in field scale with cylinder radius of 4.5m, water depth of 45 m and peak period of 13.5 seconds.

than a 3% difference with the Stokes-GP model. The FNV and Rainey models share very similar predictions in this case study, which is consistent with previous studies (Suja-Thauvin et al., 2020), as the only difference between the FNV and Rainey models is the calculation of point load.

For the higher-order harmonics, we utilise four phase decomposition method to separate out these contributions in Figure 11. We are not surprised to find both force models show better agreement with the Stokes-GP model for almost all the high frequency force components when compared to the Wheeler stretching method, especially in the fourth order in this instance, where the Wheeler stretching method predicts almost zero force amplitude. This is because both the FNV and Rainey models include all Froude-Krylov components when fully nonlinear wave kinematics are used, despite some scattering contributions from higher than third order being missing. We also report both the Rainey and FNV models predict somewhat higher second order and third order harmonic amplitudes when compared to the Stokes-GP model. For the fourth and fifth harmonics, both Rainey and FNV models show frequency-shifted results when compared to the Stokes-GP model, which could be due to the phase lag between the horizontal acceleration and load mentioned in Molin (2022).

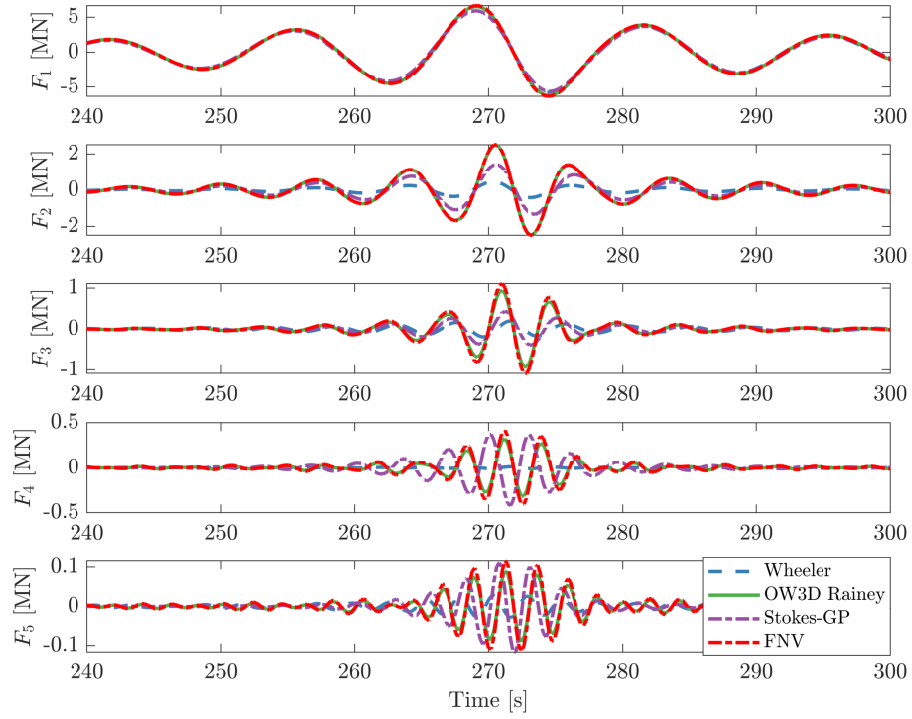


Figure 11: Comparison between Stokes-GP model (purple) and other commonly adopted nonlinear force models: Wheeler stretching method (blue), Rainey force model (green), FNV (red) calculated based on kinematics obtained from fully nonlinear potential flow simulations for higher order force harmonics obtained through phase decomposition method for a wave group at field scale with cylinder radius of 4.5m, water depth of 45 m and peak period of 13.5 seconds.

3.2. Random wave field

We apply the Stokes-GP prediction model to random time series, using a force segmentation scheme that is detailed in Appendix B. Similar approaches have been adopted in various ocean engineering applications, such as wave statistics (Farazmand and Sapsis, 2017), reduced order parameterisation (Tang and Adcock, 2022), and ship motion prediction (Gong and Pan, 2022).

We first present the Stokes-GP model prediction results for random time series in Figure 12 (a), where we find relatively accurate prediction from the model when compared with the measured total nonlinear force. We further present the difference between the model predictions and the measured force in (b). We find the overall model prediction error is almost independent of the local occurrence of extreme wave groups in the record. This suggests that our model can provide consistent predictions, even with the presence of these extreme waves as the associated higher-order harmonics are more pronounced for those large waves.

To further examine the performance of our Stokes-GP model, we performed new random wave experiments with the four-phase decomposition method in the Kelvin Hydrodynamics Laboratory at Strathclyde. The comparison between the model prediction and the nonlinear force measured during experiments is shown in Figure 13 (a). We found consistent and accurate predictions from the Stokes-GP model, which provides good estimates for the peaks in the random force series, including the extreme event presented herein. We also present the model prediction on the force peak exceedance in the mean wave direction in Figure 13 (b), where the Rayleigh distribution is also included as a reference for linear loading calculations. The proposed model captures the extra nonlinear contribution from the higher force harmonics accurately, especially for those extreme loading events out in the upper tail of the distribution.

We also included the Wheeler stretching method in Figure 13, where we calculate the Wheeler stretching with standard C_M values of 2. The Wheeler stretching method consistently over-predicts the force amplitude when compared to experimental results, especially during large loading events.

We note that it might appear that the Wheeler stretching approach is conservative (at least for the case presented here). However, this is not necessarily the case for design. As shown in Figure 11, Wheeler stretching approach does not capture the higher harmonics well and if these coincide

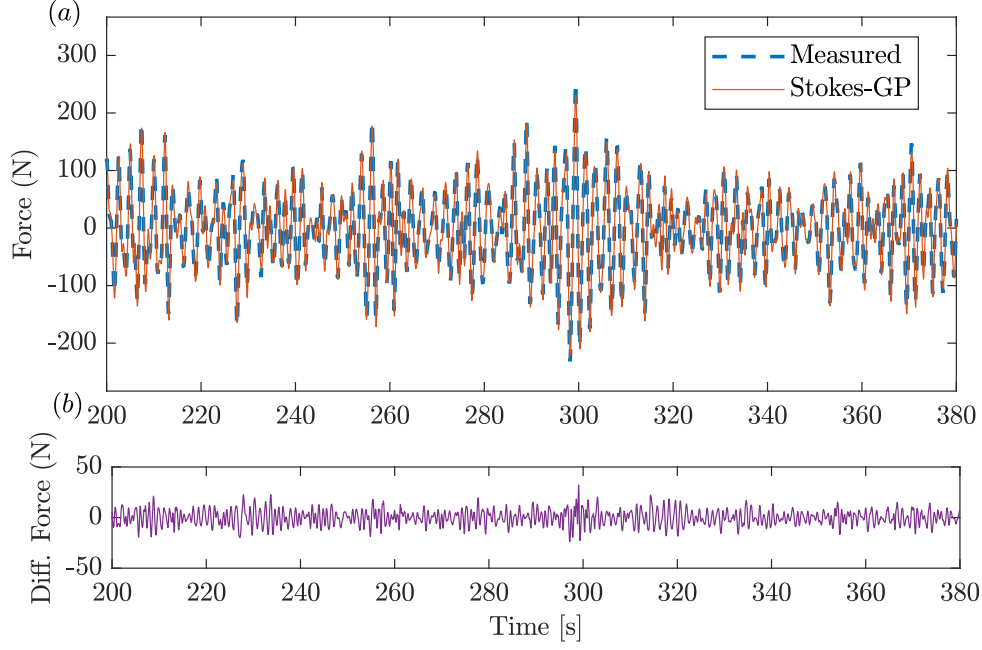


Figure 12: Wave-by-wave predictions of random force series using envelope based segmentation method and Stokes-GP model compared against measured force series in the experiment for DM3 case (a): total inline force, (b): force difference between Stokes-GP model and measured force.

with the structural resonance then the loads needed for the design of an offshore wind turbine may be under-estimated. As such, the Wheeler stretching approach could either over- or under-estimate the loads.

Finally, model prediction accuracy and reliability are of concern to engineering applications, especially for the design-critical ultimate loading conditions. Traditional data-driven methods have struggled at demonstrating model reliability due to their ‘black-box’ behaviour. However, for the Stokes-GP model presented herein, we aim to alleviate the reliability concern in two ways.

Firstly, the core of the prediction model (i.e. the Stokes-type model) is based on intuition of the non-breaking wave problem. This nonlinear force framework allows us to separate and describe higher frequency forces with force coefficients, which is ideal for interpolation by data-driven methods. More importantly, this physics-based Stokes-type model also imposes some

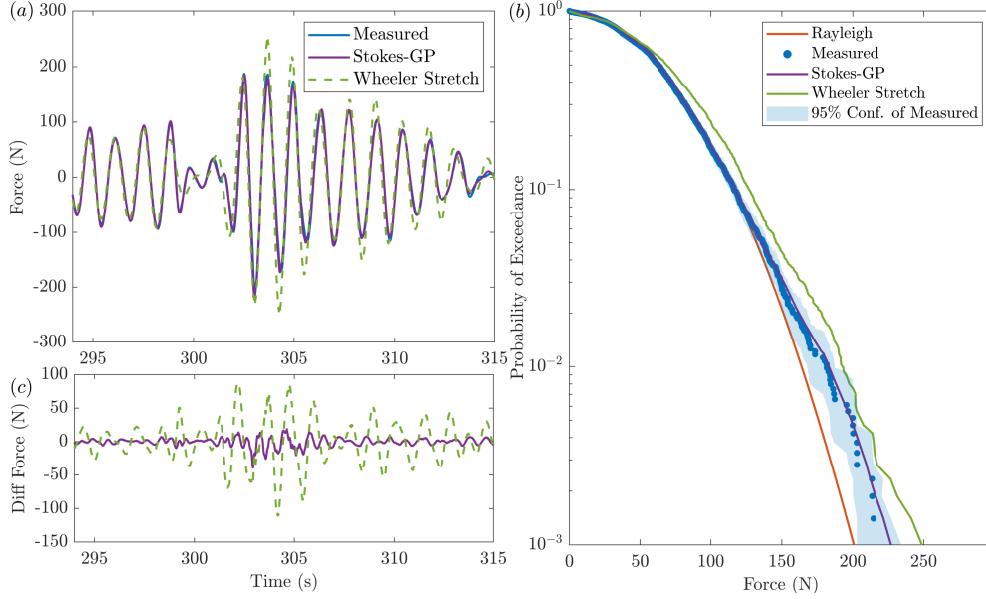


Figure 13: Stokes type model predictions of nonlinear forces compared to Wheeler Stretching method of random time series for (a): total inline forces, (b): force peak exceedance plot in the mean wave direction with $H_s = 0.10m$ and $T_p = 1.27s$, (c): force difference between Stokes-GP model, Wheeler stretching method with different C_M values and measured force.

physical constraints on these coefficients, such as these coefficients being slowly varying in the parameter space. These physical constraints are hard coded and imposed on our data-driven interpolation model at the very beginning of the model training through hyperparameters and in the model cross-validation stage, which ensures model interpolation trends agree with the underlying physics included through the Stokes type model.

Secondly, we can also leverage the use of Gaussian Processes as a statistical inference model and provide an estimation of the model reliability based on the cross-validated upper confidence interval. The confidence interval for a given GP model can be directly estimated from the covariance matrix (see Equation (C.6) in Appendix Appendix C for details). We have also utilised the k-fold cross-validation method to improve the accuracy of the uncertainty estimation and to reduce the potential for bias in the random division of training and validation data. This process involves dividing the dataset into subsets and assessing the model performance on each subset to enhance the model validity and precision (Rodriguez et al., 2009). The

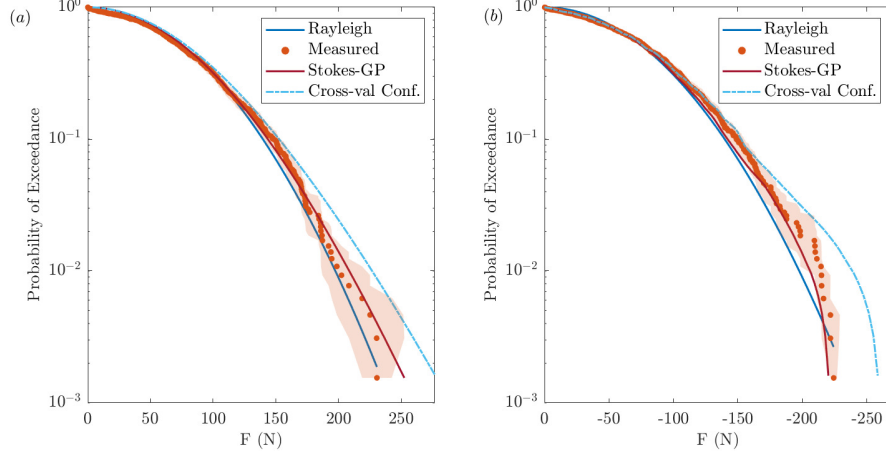


Figure 14: Force statistics of DM4 case for (a): force peak exceedance plot in mean wave direction and (b) force peak exceedance plot in opposing wave direction.

confidence intervals estimated for both peak exceedance in the mean wave direction and opposing wave direction are shown in Figure 14 based on bootstrapping, which is limited by the few large samples at the high tail of the distribution. The cross-validated upper confidence interval further takes into account some parts of the modelling uncertainty inherently associated with data interpolations with GP. This would allow a better estimation of the prediction uncertainty for engineering applications, which is unlikely to be captured by empirical line-fitting methods. We also observe a reduced departure of the force statistics in the opposing wave direction from the Rayleigh distribution for large local values, which is likely due to locally destructive out-of-phase interference between higher-order harmonics. Both the prediction model and the upper confidence interval capture this behaviour.

4. Conclusions

In this paper, we revisit the Stokes-type nonlinear force model with the aim of transforming this framework into a practical engineering prediction tool that can be integrated into the design flow of offshore monopile foundations. To achieve this, we re-analyse previous experimental results and conduct a new set of experiments at the Kelvin Hydrodynamics Laboratory to establish a database for force amplitude and phase coefficients. We find consistent coefficient values across all previous and current experimental

results, with the exception of third-order harmonics, where we suspect additional nonlinear physics may interfere with our approach. The consistent results from different datasets suggest the Stokes-type approach is relatively robust and scales well across different experimental setups.

This study also leverages various data-driven techniques, incorporating them into the physics-based Stokes-type model. These methods aid in the extraction of higher-order coefficients from experimental data, interpolation of force coefficients with limited available information, and extension of the Stokes-Gaussian Process based model application from wave groups to random time series. The integration of these data-driven techniques helps stabilise predictions for high-frequency forces with large background noise and monitors the model performance with uncertainty quantification. More importantly, these data-driven techniques provide full extensibility to this Stokes-GP model, as the prediction accuracy can be further improved with more experiments or numerical simulations feeding into the database.

There is no absolute ground truth which we can compare our experimentally derived model against. The Wheeler stretching model, commonly used in design practice, does not seem to capture the relevant physics—peak loads are over-estimated. Still, it under-estimates the load at the 2nd and higher harmonics which in many structures will correspond to the natural frequency—as such it is unclear whether or not this model is conservative. The Rainey and the FNV model, coupled with fully non-linear kinematics, appears to be better than Wheeler’s approach as would be expected from the extra physics modelled. However, the complication of generating non-linear kinematics is substantial and this method is unlikely to be practical for design. The method proposed here is computationally quick and straightforward to implement. Whilst it does make a substantial assumption about the form of the loading the results are then experimentally derived and therefore likely to be reliable. As such, we believe the proposed model strikes a balance between complexity and simplicity, which makes it highly applicable to engineering design. Work is underway to understand the sensitivity of engineering design to wave models.

Acknowledgement

This research is funded by EPSRC grant EP/V050079/1. TT is also funded by Eric and Wendy Schmidt AI in Science Postdoctoral Fellowship. We thank Henrik Bredmose of DTU for access to the Mj23 dataset, and we

also thank Harry Bingham of DTU for the use of simulation code Ocean-Wave3D.

This research was funded in whole or in part by EPSRC grant number EP/V050079/1. For the purpose of Open Access, the author has applied a CC BY public copyright licence to any Author Accepted Manuscript (AAM) version arising from this submission.

Appendix A. Past experiments details

Appendix A.1. LC18 experiments

The LC18 experimental campaign was undertaken at the Danish Hydraulic Institute (DHI), Denmark. The shallow water basin used to carry out the wave loading experiment is 35 meters long and 25 meters wide, with a constant water depth of 0.505 m. Focused wave groups were used with an energy distribution following a JONSWAP spectrum with $\gamma = 3.3$. The vertical cylinder of diameter 0.25 m was installed at 7.8 m away from the wave generators in the centre, which was supported by a stiff triangular frame with load cells at the top. During the experimental campaign, both flat bed and sloping bed were included in the experiments at 6 m upstream of the cylinder centre (see details in Chen et al. (2018)).

Incident wave groups are generated with various peak frequencies f_p and amplitude A , which can be characterized in Table A.5 for the flatbed cases. Excellent repeatability for runs with and without cylinders was confirmed by an array of wave gauges surrounding the cylinder. In this paper, we focus on the total horizontal hydrodynamic force measured by four load cells connecting the cylinder and the support frame.

During experiments, the force measured from the load cells consists of hydrodynamic forces induced by wave groups and cylinder dynamics. To remove these ‘ringing’ excitations in structural dynamics, we followed the separation method in the Fourier domain as presented in Chen et al. (2018). Under the assumption of the dynamical system of the cylinder can be approximated as a spring-mass-damper, a linear transfer function is utilised with the resonant frequency and structural damping coefficient obtained from a ‘push’ test (see further details in Chen et al. (2018)).

Appendix A.2. XF20 experiments

The second experimental campaign we considered was carried out at Kelvin Hydrodynamics Laboratory at the University of Strathclyde. The

Table A.5: Incoming wave fields for flatbed cases from Feng et al. (2020) and Chen et al. (2018), where d is water depth, and R is cylinder radius. f_p is peak frequency, k_p is the peak wavenumber and A is wave group amplitude.

Case Name	f_p [Hz]	k_p [m ⁻¹]	$k_p R$	$k_p d$	A [m]	$k_p A$
XF01	0.429	0.82	0.129	1.476	0.134	0.110
XF02	0.429	0.82	0.129	1.476	0.147	0.120
XF03	0.429	0.82	0.129	1.476	0.160	0.131
XF04	0.429	0.82	0.129	1.476	0.169	0.138
XF05	0.429	0.82	0.129	1.476	0.179	0.146
XF06	0.429	0.82	0.129	1.476	0.206	0.169
LC01	0.49	1.51	0.19	0.76	0.06	0.08
LC02	0.49	1.51	0.19	0.76	0.08	0.12
LC03	0.49	1.51	0.19	0.76	0.10	0.15
LC04	0.61	1.97	0.25	1.00	0.03	0.05
LC05	0.61	1.97	0.25	1.00	0.05	0.10
LC06	0.61	1.97	0.25	1.00	0.09	0.18
LC07	0.82	2.99	0.37	1.51	0.04	0.12
LC08	0.82	2.99	0.37	1.51	0.08	0.22
LC09	0.82	2.99	0.37	1.51	0.09	0.27
LC10	1.22	6.02	0.75	3.04	0.02	0.14
LC11	1.22	6.02	0.75	3.04	0.04	0.25
LC12	1.22	6.02	0.75	3.04	0.05	0.29

wave flume is 76 meters long, 4.6 meters wide and has a constant water depth of 1.8 meters. Wave groups were generated at one end with four ‘flap-type’ wavemakers and are absorbed by a 13 m long sloping beach at the other end. The vertical cylinder of diameter 0.315 meters was placed 35.315 meters away from the wavemaker at the centreline of the tank.

The incident wave fields generated in XF20 share the same underlying spectrum: a JONSWAP spectrum with $\gamma = 3.3$ as the previous LC18, but consists of different combinations of peak frequencies f_p and amplitudes A . The detailed parameters of incident wave groups are presented in Table A.5. The second XF2020 experimental results provide better coverage of the non-dimensionalised parameter space $(k_p A, k_p d, k_p R)$, which is critical for the nonlinear force predictions in this study. Unlike the LC18 cases, the experimental set-up in XF20 cases has a relatively high system natural frequency of 10.7 Hz when compared to the peak frequency of generated wave groups. The clear separation between the hydrodynamic forces and the system dynamics in the frequency domain suggests the ‘ringing’ response has negligible impact on the frequency range we are primarily interested in.

Appendix A.3. MJ23 experiments

The third experiment we analysed in this study was undertaken in the shallow water basin at DHI Hørsholm. A Froude scale with a geometric

Table A.6: Incoming wave fields for random waves at laboratory scale from Mj et al. (2023). H_s is significant wave height, T_p is peak wave period, γ is peak enhancement factor of the JONSWAP spectrum, d is water depth, and R is cylinder radius

Case	Water depth [m]	H_s [m]	T_p [s]	γ	kd	$kH_s/2$	kR
DM1	0.66	0.15	1.70	2.0	1.16	0.13	0.13
DM2	0.66	0.14	2.12	1.0	0.92	0.10	0.10
DM3	0.66	0.19	1.70	3.6	1.16	0.17	0.12
DM4	0.66	0.18	2.12	1.2	0.92	0.12	0.10
DM5	0.66	0.20	2.12	1.7	0.92	0.14	0.10
DM6	0.40	0.12	1.70	1.0	0.81	0.12	0.14
DM7	0.40	0.12	1.84	1.0	0.74	0.11	0.13
DM8	0.40	0.14	1.70	1.6	0.81	0.14	0.14
DM9	0.40	0.14	1.98	1.0	0.68	0.12	0.12
DM10	0.40	0.15	1.98	1.0	0.68	0.13	0.12
DM11	0.40	0.11	1.27	4.3	1.21	0.17	0.21

length scaling ratio of 1:50 was applied in the original paper (Bredmose et al., 2016), whereas we present the laboratory scale for consistency with other experimental results.

The cylinder with a radius of 0.07 m was used in this experimental campaign and was installed at a distance of 7.3 m from the wave paddles during the experimental campaign. Two water depths (0.4 m and 0.66 m) are considered. The inline force time series are measured by force transducers at the top and bottom of the cylinder with a sampling frequency of 256 Hz. The natural frequency of the system is estimated to be over 3 Hz, and the dynamic structural responses are well separated from the hydrodynamic loading in the frequency domain.

As opposed to focused wave groups generated in LC18 and XF20, we explore unidirectional random waves in MJ23 with wave steepness varying from 0.1 to 0.17. The peak enhancement factor γ of the JONSWAP spectrum is also varied to reflect a wider range of sea states with different bandwidths in the ocean. The detailed wave field parameters can be found in Table A.6.

Appendix B. Envelope based random time series segmentation

In this paper, we segment the random time series based on a data-driven envelope method presented in Farazmand and Sapsis (2017). This segmentation improves the extension of our Stokes-GP model to random series predictions. This segmentation has two steps. We first obtain the local force envelope peak by obtaining the local maximum points. We further followed

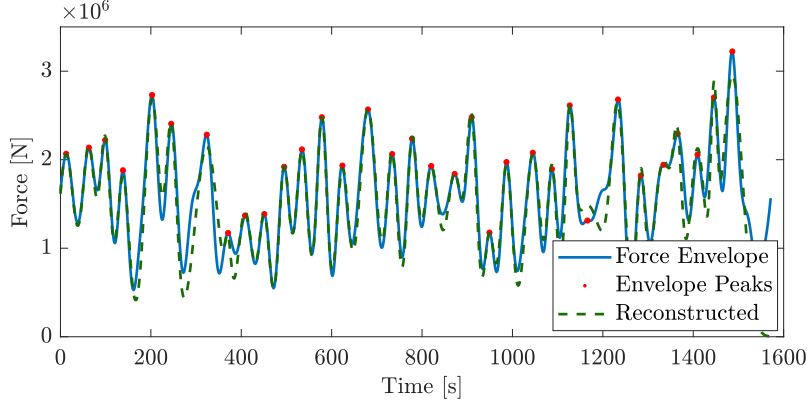


Figure B.15: Gaussian force envelope based wave group detection method for case DM04.

Farazmand and Sapsis (2017) and approximated the force series as a superposition of Gaussian force envelopes:

$$B_0(t) = \sum_1^n B_n \exp \left(\frac{(t - T_{c,n}^2)^2}{T_{t,n}^2} \right), \quad (\text{B.1})$$

where $B_0(t)$ is the reconstructed envelope, B_n is the amplitude of the n^{th} Gaussian envelope, $T_{c,n}$ is the centre of the envelope obtained through envelope peak and $T_{t,n}$ is a length scale parameter, which can be estimated by minimising the differences between the force envelope field and the superposition approximation (see details in Tang and Adcock (2022)).

From Figure B.15, the proposed envelope decomposition method can successfully approximate the random force envelope with the superposition of Gaussian envelopes. This provides accurate guidance on splitting the entire random series into individual wave groups, which enables accurate prediction of random wave statistics from a model that is trained on individual wave groups. This approach also leverages the challenges when estimating the peak wavenumber for random waves as each isolated wave groups have its own peak wavenumber, which also improves the model prediction accuracy.

Appendix C. Gaussian Process method and hyper parameter optimisation

In this study, we describe the variation of force amplitude coefficients $\Gamma(x)$ with three non-dimentionalised parameters $k_p A$, $k_p d$ and $k_p R$ with a GP

model (\mathcal{GP}) using a mean function $m(x)$ and a covariance function $k(x, x^*)$:

$$\begin{aligned}\Gamma(x) &\sim \mathcal{GP}(m(x), k(x, x^*)) \\ m(x) &= \mathbb{E}[\Gamma(x)] \\ k(x, x^*) &= \text{cov}(\Gamma(x), \Gamma(x^*))\end{aligned}\tag{C.1}$$

where $x \in (k_p A, k_p d, k_p R)$ is a parameter space input vector with three dimensions, $\Gamma(x)$ and $\Gamma(x^*)$ are force amplitude coefficients response indexed by x and x^* . Generally, $k(x, x^*)$ is also referred to as a kernel function, which is further parameterised by hyperparameter θ .

The Gaussian Process approach is a common Bayesian non-parametric model used for both regressions and parameterisation purposes. This method is particularly suitable in our prediction model because of its strong resistance to under-fitting the problems. In this study, one of the key challenges for accurate prediction of force coefficients is the limited data available from previous experiments. A GP's expressiveness in proportion to the size and complexity of the growing dataset avoids the under-fitting problem (Durbin and Koopman, 2012) for small datasets. Additionally, the ability to provide uncertainty quantifications based on the prior the modelled system also in favours the wide application of the GP model in many engineering problems, such as system identification (Kocijan et al., 2004), control (Hewing et al., 2019) and forecasting (Gramstad et al., 2020).

In this study, the variation function of force amplitude coefficients $\Gamma(x)$ in parameters space $x \in (k_p A, k_p d, k_p R)$ is assumed to be a complex system without existing expert domain knowledge. For systems without any accurate description for the dynamics model, a GP model is commonly initialised with a zero mean function, which leads to the prior in GP being solely dependent on the choice of the covariance function $k(x, x^*)$. Although the covariance function $k(x, x^*)$ is fully customisable for any function, which can provide a positive definite covariance matrix, the selection of this function determines the periodicity and smoothness of the trained GP model. Hence, a suitable covariance function type and hyperparameter θ initial values are required during the initialisation of a GP prior.

In this study, we follow the most common covariance function: squared exponential, which is also noted as Radial Basis Function:

$$k(x_i, x_j) = h_1^2 \exp \left[- \left(\frac{x_i - x_j}{\lambda} \right)^2 \right], \tag{C.2}$$

where there are two hyperparameters $\boldsymbol{\theta} = (h, \lambda)^T$. The hyperparameters determine the smoothness of the covariance function, which can be further optimised by using a loss function based on log marginal likelihood function following Rasmussen and Williams (2006):

$$\log p(y | \boldsymbol{\theta}) = -\frac{1}{2} \log |K| - \frac{1}{2} y^T K^{-1} y - \frac{n}{2} \log(2\pi), \quad (\text{C.3})$$

where K is the covariance matrix, which stores the correlations between input points:

$$K = \begin{bmatrix} k(x_1, x_1) & k(x_1, x_2) & \cdots & k(x_1, x_N) \\ k(x_2, x_1) & k(x_2, x_2) & \cdots & k(x_2, x_N) \\ k(x_3, x_1) & k(x_3, x_2) & \cdots & k(x_3, x_N) \\ \vdots & \vdots & \ddots & \vdots \\ k(x_N, x_1) & k(x_N, x_2) & \cdots & k(x_N, x_N) \end{bmatrix} \quad (\text{C.4})$$

and n is the number of observations presented in the dataset, and the $p(y | \boldsymbol{\theta})$ is the conditional distribution of latent function at the provided observations.

To optimise the log marginal likelihood based loss function, a standard gradient decent converging algorithm is applied for non-convex optimisation with suitable initial value of hyperparameters estimated from a coarse grid search. This precondition process allows faster convergence during optimisation and minimised the likelihood of converging to an undesirable local optima.

The trained GP model can make the prediction Γ^* for a new given input X^* based on the extended joint distribution as:

$$\begin{bmatrix} \Gamma^* \\ y \end{bmatrix} \sim \left(\begin{bmatrix} m(X^*) \\ m(X) \end{bmatrix}, \begin{bmatrix} k(X^*, X^*) & k(X^*, X) \\ k(X, X^*) & K + \sigma^2 I \end{bmatrix} \right) \quad (\text{C.5})$$

where $k(X^*, X) = k(X, X^*)^T = [k(X_1, X^*), \dots, k(X_N, X^*)]$, X are observation datasets, σ^2 is the noise variance, and I is the identity matrix.

According to the properties of joint Gaussian distributions, the prediction results for the outputs can be obtained as:

$$\begin{aligned} \mu(\Gamma^*) &= m(X^*) + k(X^*, X) [K + \sigma^2 I]^{-1} (Y - m(X)) \\ \text{var}(\Gamma^*) &= k(X^*, X^*) - k(X^*, X) [K + \sigma^2 I]^{-1} k(X, X^*), \end{aligned} \quad (\text{C.6})$$

where $\mu(\Gamma^*)$ is the predicted force amplitude coefficients and $\text{var}(\Gamma^*)$ is the variance of the predicted force amplitude coefficients.

For a limited size of dataset, the random split of the training and validation data may also introduce bias in the prediction results. To minimise the impact of this split, bootstrapped k-fold cross-validation process Rodriguez et al. (2009) is applied to further examine the accuracy of our GP model. In this study, the dataset is uniformly divided into n subsets and $n - 1$ uniform-sized subsets are used for GP model training. The performance of the current trained GP model can be evaluated by validating against the out-of-bag sample. After repeating the training and validation process covering all the data points as the out-of-bag sample, the overall performance measurements can be calculated as the average across the k-folds.

References

- Adcock, T.A.A., Feng, X., Tang, T., van den Bremer, T.S., Day, S., Dai, S., Li, Y., Lin, Z., Xu, W., Taylor, P.H., 2019. Application of phase decomposition to the analysis of random time series from wave basin tests, in: International Conference on Offshore Mechanics and Arctic Engineering, American Society of Mechanical Engineers. p. V009T12A020.
- Adcock, T.A.A., Yan, S., 2010. The focusing of uni-directional Gaussian wave-groups in finite depth: an approximate NLSE based approach. 29th Int. Ocean Offshore Arct. Eng. Conf., Shanghai, China 49125, 569–576.
- Baldock, T.E., Swan, C., Taylor, P.H., 1996. A laboratory study of nonlinear surface waves on water. *Philos. Trans. Royal Soc. A Math. Phys. Eng. Sci.* 354, 649–676.
- Bredmose, H., Dixen, M., Ghadirian, A., Larsen, T.J., Schløer, S., Andersen, S., Wang, S., Bingham, H.B., Lindberg, O., Christensen, E.D., Vested, M.H., S, C., Engsig-Karup, A.P., Petersen, O.S., Hansen, H.F., Mariegaard, J.S., Taylor, P.H., Adcock, T.A.A., Obhrai, C., Gudmestad, O.T., Tarp-Johansen, N.J., Meyer, C.P., Krokstad, J.R., Suja-Thauvin, L., Hanson, T.D., 2016. DeRisk-accurate prediction of ULS wave loads. outlook and first results. *Energy Procedia* 94, 379–387.
- Chaplin, J.R., 1996. On frequency-focusing unidirectional waves. *International Journal of Offshore and Polar Engineering* 6.

- Chaplin, J.R., Rainey, R.C.T., Yemm, R.W., 1997. Ringing of a vertical cylinder in waves. *Journal of Fluid Mechanics* , 119–147.
- Chen, L.F., Zang, J., Taylor, P.H., Sun, L., Morgan, G.C.J., Grice, J., Orszaghova, J., Ruiz, M.T., 2018. An experimental decomposition of nonlinear forces on a surface-piercing column: Stokes-type expansions of the force harmonics. *Journal of Fluid Mechanics* 848, 42–77.
- Durbin, J., Koopman, S.J., 2012. *Time Series Analysis by State Space Methods*. volume 38. OUP Oxford.
- Eatock Taylor, R., Chau, F.P., 1991. Wave diffraction-some developments in linear and non-linear theory. *Journal of Offshore Mechanics and Arctic Engineering* 1, 19.
- Eatock Taylor, R., Hung, S.M., 1987. Second order diffraction forces on a vertical cylinder in regular waves. *Applied Ocean Research* 9, 19–30.
- Engsig-Karup, A.P., Bingham, H.B., Lindberg, O., 2009. An efficient flexible-order model for 3D nonlinear water waves. *J. Comput. Phys.* 228, 2100–2118.
- Esandi, J.M., Buldakov, E., Simons, R., Stagonas, D., 2020. An experimental study on wave forces on a vertical cylinder due to spilling breaking and near-breaking wave groups. *Coast. Eng.* 162, 103778.
- Faltinsen, O.M., Newman, J.N., Vinje, T., 1995. Nonlinear wave loads on a slender vertical cylinder. *Journal of Fluid Mechanics* 289, 179–198.
- Farazmand, M., Sapsis, T.P., 2017. Reduced-order prediction of rogue waves in two-dimensional deep-water waves. *Journal of Computational Physics* 340, 418–434.
- Feng, X., Taylor, P.H., Dai, S., Day, A.H., Willden, R.H.J., Adcock, T.A.A., 2020. Experimental investigation of higher harmonic wave loads and moments on a vertical cylinder by a phase-manipulation method. *Coastal Engineering* 160, 103747.
- Fitzgerald, C.J., Taylor, P.H., Eatock Taylor, R., Grice, J., Zang, J., 2014. Phase manipulation and the harmonic components of ringing forces on a surface-piercing column. *Proceedings of the Royal Society A: Mathematical, Physical Engineering and Science* 470, 20130847–20130847.

- Gong, X., Pan, Y., 2022. Sequential bayesian experimental design for estimation of extreme-event probability in stochastic input-to-response systems. *Computer Methods in Applied Mechanics and Engineering* 395, 114979.
- Gramstad, O., Agrell, C., Bitner-Gregersen, E., Guo, B., Ruth, E., Vanem, E., 2020. Sequential sampling method using gaussian process regression for estimating extreme structural response. *Marine Structures* 72, 102780.
- Grue, J., Huseby, M., 2002. Higher-harmonic wave forces and ringing of vertical cylinders. *Applied ocean research* 24, 203–214.
- Gupta, B.K., Basu, D., 2020. Offshore wind turbine monopile foundations: Design perspectives. *Ocean Engineering* 213, 107514.
- Hewing, L., Kabzan, J., Zeilinger, M.N., 2019. Cautious model predictive control using gaussian process regression. *IEEE Transactions on Control Systems Technology* 28, 2736–2743.
- Huseby, M., Grue, J., 2000. An experimental investigation of higher-harmonic wave forces on a vertical cylinder. *Journal of fluid Mechanics* 414, 75–103.
- International Electrotechnical Commission, 2009. 61400-3, Wind turbines-part 3: Design requirements for offshore wind turbines. International Electrotechnical Commission, Geneva .
- Jiang, C., el Moctar, O., 2022. Numerical investigation of wave-induced loads on an offshore monopile using a viscous and a potential-flow solver. *Journal of Ocean Engineering and Marine Energy* 8, 381–397.
- Kocijan, J., Murray-Smith, R., Rasmussen, C.E., Girard, A., 2004. Gaussian process model based predictive control, in: *Proceedings of the 2004 American control conference, IEEE*. pp. 2214–2219.
- Kristiansen, T., Faltinsen, O.M., 2017. Higher harmonic wave loads on a vertical cylinder in finite water depth. *Journal of Fluid Mechanics* 833, 773–805.
- Malekjafarian, A., Jalilvand, S., Doherty, P., Igoe, D., 2021. Foundation damping for monopile supported offshore wind turbines: A review. *Marine Structures* 77, 102937.

- Malenica, Š., Clark, P.J., Molin, B., 1995. Wave and current forces on a vertical cylinder free to surge and sway. *Applied Ocean Research* 17, 79–90.
- Mj, D., McAllister, M.L., Bredmose, H., Adcock, T.A.A., Taylor, P.H., 2023. Harmonic structure of wave loads on a surface piercing column in directionally spread and unidirectional random seas. *Journal of Ocean Engineering and Marine Energy* , 1–19.
- Molin, B., 1979. Second-order diffraction loads upon three-dimensional bodies. *Applied Ocean Research* 1, 197–202.
- Molin, B., 2022. *Offshore Structure Hydrodynamics*. Cambridge University Press.
- Nestegård, A., Ronæss, M., Hagen, Ø., Ronold, K.O., Bitner-Gregersen, E.M., 2006. New DNV Recommended Practice DNV-RP-C205 On Environmental Conditions And Environmental Loads.
- Newman, J.N., 1996. Nonlinear Scattering of Long Waves by a Vertical Cylinder. Springer Netherlands, Dordrecht. pp. 91–102.
- Rainey, R.C.T., 1995. Slender-body expressions for the wave load on offshore structures. *Proceedings of the Royal Society of London. Series A: Mathematical and Physical Sciences* 450, 391–416.
- Rasmussen, C.E., Williams, C., 2006. Gaussian processes for machine learning, adaptive computation and machine learning. Cambridge, MA, USA: MIT Press 38, 715–719.
- Riise, B.H., Grue, J., Jensen, A., Johannessen, T.B., 2018. High frequency resonant response of a monopile in irregular deep water waves. *Journal of Fluid Mechanics* 853, 564–586.
- Rodriguez, J.D., Perez, A., Lozano, J.A., 2009. Sensitivity analysis of k-fold cross validation in prediction error estimation. *IEEE Trans. Pattern Anal. Mach. Intell.* 32, 569–575.
- Ruder, S., 2016. An overview of gradient descent optimization algorithms. arXiv preprint arXiv:1609.04747 .

- Schlører, S., Bredmose, H., Bingham, H.B., 2016. The influence of fully non-linear wave forces on aero-hydro-elastic calculations of monopile wind turbines. *Marine Structures* 50, 162–188.
- Stansberg, C.T., Huse, E., Krokstad, J.R., Lehn, E., 1995. Experimental study of non-linear loads on vertical cylinders in steep random waves. The Fifth International Offshore and Polar Engineering Conference, The Hague, The Netherlands , 824.
- Suja-Thauvin, L., Bachynski, E.E., Pierella, F., Borg, M., Krokstad, J.R., Bredmose, H., 2020. Critical assessment of hydrodynamic load models for a monopile structure in finite water depth. *Marine Structures* 72, 102743.
- Tang, T., Adcock, T.A.A., 2022. A reduced order model for space–time wave statistics using probabilistic decomposition–synthesis method. *Ocean Engineering* 259, 111860.
- Tang, T., Ding, H., Dai, S., Chen, X., Taylor, P.H., Zang, J., Adcock, T.A., 2023a. Data informed model test design with machine learning-an example in nonlinear load on vertical cylinder, in: ASME 2023 42nd International Conference on Ocean, Offshore and Arctic Engineering.
- Tang, T., Ding, H., Dai, S., Chen, X., Taylor, P.H., Zang, J., Adcock, T.A.A., 2023b. Data informed model test design with machine learning - an example in nonlinear wave load on a vertical cylinder. *Proceedings of the 42nd International Conference on Ocean, Offshore and Arctic Engineering (OMAE 2023)*, Melbourne, Australia .
- Tromans, P., Swan, C., Masterton, S., 2006. Nonlinear potential flow forcing: the ringing of concrete gravity based structures. *Health and Safety Executive Report*, UK .
- Wang, S., Larsen, T.J., Bredmose, H., 2021. Ultimate load analysis of a 10 MW offshore monopile wind turbine incorporating fully nonlinear irregular wave kinematics. *Marine Structures* 76, 102922.
- Wheeler, J.D., 1970. Method for calculating forces produced by irregular waves. *J. Pet. Technol.* 22, 359–367.
- Zang, J., Gibson, R., Taylor, P.H., Eatock Taylor, R., Swan, C., 2006. Second order wave diffraction around a fixed ship-shaped body in unidirectional steep waves. *Journal of Offshore Mechanics and Arctic Engineering* , 89–99.